Thermal Science and Engineering Progress 55 (2024) 102901

Contents lists available at ScienceDirect

Thermal Science and Engineering Progress

journal homepage: www.sciencedirect.com/journal/thermal-science-and-engineering-progress

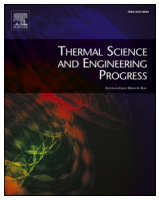

Numerical simulation of a laser beam welding process: From a thermomechanical model to the experimental inspection and validation

O. Murua [a,*], J.I. Arrizubieta [a], A. Lamikiz [a], H.I. Schneider [b]

[a] Department of Mechanical Engineering, University of the Basque Country UPV/EHU, Plaza Torres Quevedo 1, 48013 Bilbao, Spain
[b] Siemens AG DI MC AMF, Freyeslebenstraße 1, 91058 Erlangen, Germany

ARTICLE INFO

Keywords:
Numerical simulation
Laser beam welding
Thermomechanical model
Experimental validation

ABSTRACT

In laser beam welding (LBW) complex physical phenomena occur during laser-material interaction, which prolong the parameterisation of the process due to the extended trial and error tests. Therefore, predicting the process behaviour leads to a more productive and cost-reduced process experimental tuning. Besides, as LBW is a thermal process, part distortion plays a relevant role in the final result, and hence, thermal and mechanical analysis are both required. In view of this, in the present research, a novel multiscale numerical model, capable of predicting the thermomechanical behaviour of the LBW process has been developed. The significance of the model is its capability of forecasting the part distortion and thermal field employing two fully coupled modules, where the laser heat source automatically adapts to the welding regime without the need to consider the melt pool dynamics and at a low computational cost. The local model determines the melt pool dimensions and thermal field. Besides, the second module, the global model, figures out the part distortion based on the thermal results. Finally, the presented numerical simulations are experimentally validated with the corresponding temperature monitoring during the welding process, the posterior metallography inspection, and the part deformation measurement. The results present a high accuracy, with a maximum error below 10 % at the temperature measurements, an average dimensional deviation of 0.14 mm and 0.18 mm respectively for the weld bead depth and width, and a vertical deformation average error of 0.15 mm.

1. Introduction

Laser beam welding (LBW) has been used since the early stage of laser material processing in 1960s as an effective technique for high-quality welding. Besides, over the last years developments in laser equipment, such as the appearance of high-power lasers, have made it possible to switch from conduction to keyhole welding and obtain high-aspect-ratio and deep penetration joints [1]. Moreover, the use of a laser source offers the advantages of high flexibility, low heat-affected zone, high repeatability, and high processing speed [2].

The above-detailed advantages make LBW suitable for welding aeroengine components, typically made of nickel-based superalloys. These materials need to withstand high mechanical loads in combination with thermal stresses, and one of the most employed is the Inconel 718 [3]. This alloy offers excellent oxidation and corrosion resistance, combined with an adequate welding capability in terms of strength and ductility [4].

Given the capabilities of LBW for joining superalloys such as the Inconel 718, successive models have been developed to increase the process knowledge and rise productivity. For instance, Fisk and Lundbäck presented a Finite Elements Method (FEM) for welding Inconel 718 plates to facilitate a first-hit design of the welding shape, and good preliminary results according to experimental tests were achieved [5]. However, simulation of LBW is still challenging because of the complexity and interrelation of the individual physical phenomena that occur during LBW [6]. Consequently, simplifying hypotheses and neglecting some phenomena is a typical practice in most models [7]. For example, one of the most common simplifications is the assumption of temperature-independent material properties [8]. Ki et al. presented a two-chapter study about keyhole modelling to determine the influence of the different assumptions such as omitting the vaporisation, and reflections, although the material properties depended only on the state of matter and were temperature-independent [9,10].

Most research works focus on determining the melt pool generated by the laser, where the heat input is experimentally calibrated for each situation. For instance, Farroki et al. presented a double three-

* Corresponding author.
E-mail address: oihane.murua@ehu.eus (O. Murua).

https://doi.org/10.1016/j.tsep.2024.102901
Received 8 February 2024; Received in revised form 5 September 2024; Accepted 14 September 2024
Available online 19 September 2024

dimensional thermal model of keyhole welding, concluding that two or more volumetric models of heat source must be combined to obtain the correct shape of the melted area [11]. In parallel, Zhang et al. [12] and Ai et al. [13] also reached the same conclusion after developing a model that considered the melt pool dynamics.

The inclusion or omission of melt pool dynamics in the development of an LBW model is one of the main debates, as its inclusion increases the computational cost drastically. Fotovvati et al. indicated that the inclusion of the melt pool dynamics is interesting when the thermal field and the weld bead dimensions are to be evaluated [14]. In the same line, Saldi et al. stated that if the melt pool dynamics are not included in a model, alternatives such as enhancing the diffusivity factor of the melt pool need to be included to obtain accurate results [15]. Feng et al. also studied the influence of the molten material dynamics and concluded that such phenomenon could be considered as steady and regular for stable welds [16]. This result was previously stated by Oreper et al., who concluded that when a large pool of melt is formed, its dynamics must be considered, although for certain conduction welds, e.g. LBW, such dynamics can be neglected [17]. This fact opens the door to the development of numerical models that do not include the melt pool dynamics itself, but introduce a welding regime depending on absorptivity or a variable heat source among other strategies. Ebrahimi et al. for instance developed a model in which five different methods for the heat source implementation were considered and concluded that employing physically realistic heat sources as well as temperature-dependent properties is the best modelling approach [18]. In this field, researchers like Li et al. have demonstrated that an accurate LBW model is feasible without accounting for the dynamics [19].

Regarding the laser as a heat source, Shehryar Khan et al. evaluated the effect of laser beam defocusing in LBW. In such paper, a FEM was developed, and they concluded that focussing the laser beam inside the part produces a weld bead change from X-shape to Y-shape [20]. However, the model does not consider the melt-pool dynamics, and the welding regime (conduction or keyhole) needs to be known beforehand since a predetermined volumetric heat source is employed. Typically, in laser welding models the heat source is preestablished by the user, which are the cases of Zhang et al. [12] and Ai et al. [13].

Other authors like Hernando et al. have included effects such as the wobble strategy in LBW and predicted the weld bead and microstructure in Inconel 718 plates [21]. Still, the mechanical behaviour of the joints was not analysed, which is essential if a complete LBW model is to be obtained [22]. Besides, only a fraction of the weld bead was simulated to reduce the computational cost, this approach is not valid for multiple or long welds and to study their thermomechanical behaviour.

During the LBW process, the deformations of the plates can have a significant influence in the results, since the weld joint can result out of tolerances or even cracked. Additionally, the laser beam could be defocused, leading to a loss of the optimal parameters. Nevertheless, the prediction of the LBW distortions is a complex task; thus, process digitalization is becoming more and more relevant. Overall, the thermomechanical models have a high computational cost and intending to reduce this, Granell et al. developed a model that divided the weld bead into sections of different lengths. They were successful in predicting the deformations, although the outcomes presented a 20 % discrepancy with the experimental results [23]. In this area, Jia et al. presented a thermomechanical LBW numerical model with its corresponding experimental validation. The numerical results were well correlated with the experimental tests, and they concluded that the weld deformation of the plate is mainly related to the welding speed [24]. However, they did not take into account that the welding speed is also responsible for the welding regime. Therefore, there is still room for improvement.

Nowadays, grounded on the increasing capability of computers, more complex numerical models are being developed, which provide the opportunity to digitalize the LBW process. The key factor for a well-programmed model is to fully identify the main aspects of the process to reduce the computational cost associated with the non-relevant parameters. Precisely, in LBW the melting and solidification process is controlled by the melt pool characteristics, the keyhole formation, the temperature distribution, and the absorptivity variations [25]. Besides, the several complex physical phenomena that are involved in LBW are the reason why monitoring systems are required for ensuring the weld quality [26]. For instance, Luo et al. used a coaxial camera with a posterior image processing tool to develop an online weld pool monitoring system [27]. In order to obtain the maximum temperatures reached during the LBW process, a pyrometer is a suitable tool, moreover, based on the temperature signal the welding mode and different defects can be identified [28]. Another monitoring system is spectroscopy, which enables to identify internal defects in order to define the optimal welding parameters [29]. Nevertheless, this last system presents a higher cost than the others in terms of the accuracy it offers [26].

In view of the state of the art, the present research aims to develop a model of the LBW process for forecasting its behaviour and the final weld bead properties. The novelty of the developed model lies in a multiscale approach which shortens the calculation time and provides the thermal and mechanical results of the LBW process with high accuracy. In addition, opposed to the investigations where the heat source needed to be previously user-defined, the model detects the welding mechanism and automatically adjusts the heat source of the laser accordingly. This way, it enables the laser beam to penetrate the substrate during keyhole welding, providing good geometrical correlation with the experimental weld bead at a low computational cost. For such purpose, the core of the thermomechanical model is composed of two main modules, called global and local, which are fully coupled to simulate the LBW process at different scales. The global model is aimed at calculating the thermal field and the resulting deformations, whereas the local model calculates the melt pool size and the maximum temperatures. In addition, an experimental monitoring system is implemented to validate the model. Finally, a case study is performed to validate the numerical simulations, including the inspection of the cross-sections of the weld beads.

2. Methodology

The methodology applied for the three-dimensional multiscale LBW model focuses on obtaining a computationally competent model with an acceptable accuracy. The flux diagram of the complete model is

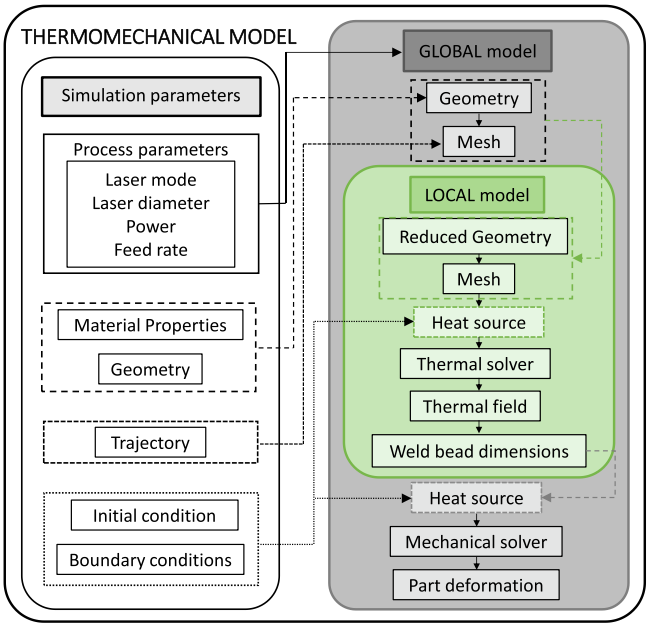

Fig. 1. The flux diagram of the thermomechanical model.

displayed in Fig. 1.

The multiscale nature of the model enables the simulation of larger components at an affordable computational cost. Besides, the welding mode dependent heat source allows to simulate different welding regimens without the need to consider the molten material movement. The local model, LM, is aimed at obtaining the weld geometry and the melt pool temperature field by solving the thermal model described in section 3.2. Therefore, the LM is defined at the weld bead scale. In contrast, the global model, GM, evaluates the heat dissipation and temperature gradient in the whole component, where the weld bead dimensions are defined based on the LM model results. In addition, the GM simulates the mechanical behaviour of the part considering the material shrinkage during the cooling stage, see section 3.3.

Therefore, the GM simulates the geometry of the whole component, while the LM extracts a portion of the geometry, allowing a thinner mesh to be used and increasing accuracy at a lower computational cost. Moreover, the differences between both models go beyond their size. In the LM the real laser beam is defined as the heat input, whereas in the GM the weld beads are simulated as a whole, and the equivalent energy input is introduced, as indicated in section 3.6. This way the computational cost is considerably reduced, and larger weld beads can be simulated at no extra cost.

The numerical simulation starts by defining the simulation parameters, see the left column in Fig. 1. These parameters are divided into 4 groups including process parameters, weld plate geometry and material, trajectory, and initial and boundary conditions. Upon defining all the necessary input parameters, the simulation of the model proceeds by loading the geometry of the GM and its subsequent meshing, see the right column in Fig. 1. For solving the LM, its geometry is first extracted from the GM and meshed. Afterwards, the LM is solved by uploading the initial and boundary conditions. Once the thermal field and weld bead dimensions are obtained in the LM, the thermal and mechanical problems are solved in the GM, which provides resulting part deformation.

3. Mathematical modelling

The finite element model (FEM) is developed using the commercial software Matlab R2023a, where the Partial Derivative Equation (PDE) Toolbox is employed. Based on the toolbox capabilities, the model does not consider the movement of the molten material but includes material elimination once it is vaporised in order to simulate the keyhole welding.

3.1. Model assumptions

The model is based on a number of simplifying hypotheses. The aim is to reduce the computational effort while minimising their impact on the results. Hereafter, these assumptions are listed and justified:

- The material properties, such as the density, the thermal diffusivity, and the specific heat are temperature dependent.
- The material is isotropic and homogeneous; thus, it is continuous.
- Melt-pool dynamics and material movement inside the melt pool are omitted to avoid solving the fluid-dynamic equations and to reduce the computational cost. This assumption is based on the conclusion reached by Feng et al, who stated that in a stable welding regime generated by an appropriate shielding gas set-up, a constant behaviour of the melt pool dynamics can be considered [16]. Moreover, this approach of omitting the melt pool dynamics has been successfully employed by Li et al., who presented an LBW model capable of predicting accurately the melt pool temperatures and weld dimensions [19].
- The absorptivity depends mainly on the laser characteristics, the laser beam incident angle, the surface temperature, and the surface material properties [30] and typically tends to increase linearly with the temperature [31]. However, Santine-Catherine et al. measured experimentally that the Inconel 718 presents a rather stable absorptivity value at different temperatures [32], what justifies employing a constant absorptivity value during conduction welding. Consequently, in the present model, the absorptivity of the Inconel 718 is set to 0.4 for a fibre laser and a normal incidence angle while conduction welding is taking place [33]. Moreover, incidence angle variations below 40° are reported to have a negligible effect on the absorptivity [34].
- In the present model when the welding mode changes from conduction to keyhole, the absorptivity is increased up to the unit to consider the augmented energy transfer efficiency due to the multiple reflections [35].
- Considering that the actual machines have a trajectory smoothing algorithm, the model neglects the acceleration and deceleration effects of the laser machine.
- The mechanical model considers the volumetric contraction of the material as the weld bead cools down from fusion temperature to room temperature.

3.2. Basis of the thermal model

The model solves the heat transfer problem by implementing the Fourier's law, Eq. (1), where k is the thermal conductivity of the material, $T = T(\{u\}, t)$ is the temperature distribution, and $q = q(\{u\}, t)$ is the heat flux at a given position $\{u\} = \{xyz\}$ and time step t.

$$q = -k \bullet \nabla T \tag{1}$$

As the heat problem is transient, the first equation of thermodynamics must be applied. Therefore, the transient heat transfer partial derivative equation (PDE), Eq. (2), is evaluated based on the finite element method, where ρ is the material density, C_p is the specific heat, k is the thermal conductivity, T is the temperature, and f is the generated heat.

$$\rho \bullet C_p \bullet \frac{\partial T}{\partial t} - \nabla \bullet (k \bullet \nabla T) = f \tag{2}$$

The solution of Eq. (2) is given for a mesh in the domain Ω and a positive time (t > 0). Additionally, the temperature vector can be split into two variables to facilitate further calculations. Being the variable separation focused on the position vector $\{u\}$ and the time t, the respective variables are $M_i(\{u\})$ and $G_i(t)$ which are represented in Eq. (3).

$$T(\{u\}, t) = \sum_{i=1}^{N} M_i(\{u\}) \bullet G_i(t) \tag{3}$$

After applying the variable separation, Eq.4 is multiplied by a continuous function over the entire domain, N_j, and the product is integrated into the whole domain Ω, see Eq. (5).

$$\rho \bullet C_p \bullet \frac{\partial (M_i \bullet G_i)}{\partial t} - \nabla \bullet (k \bullet \nabla (M_i \bullet G_i)) = f \tag{4}$$

$$\int_{\Omega} \left[\rho \bullet C_p \bullet M_i \bullet \frac{\partial G_i}{\partial t} \right] \bullet N_j d\Omega + \int_{\Omega} [- \nabla \bullet (k \bullet \nabla (M_i \bullet G_i))] \bullet N_j d\Omega = \int_{\Omega} f \bullet N_j d\Omega \tag{5}$$

By multiplying the gradients of the second integral, the resultant expression is simplified as shown in Eq. (6).

$$\int_{\Omega} \left[\rho \bullet C_p \bullet M_i \bullet \frac{\partial G_i}{\partial t} \right] \bullet N_j d\Omega + \int_{\Omega} \left[-k \bullet \left(\nabla^2 M_i \bullet N_j \right) \bullet G_i \right] d\Omega = \int_{\Omega} f \bullet N_j d\Omega \tag{6}$$

Since Green's first identity is a special case of the divergence theorem, it

is then applied in Eq. (7) to evaluate the result of the product rule, where $\hat{n}$ is the normal vector to the boundary, $\partial\Omega$, along which the boundary condition is being applied.

$$\int_{\Omega}\left[\rho \bullet C_p \bullet M_i \bullet \frac{\partial G_i}{\partial t}\right] \bullet N_j d\Omega + \int_{\Omega}\left[k \bullet \left(\nabla M_i \bullet \nabla N_j\right) \bullet G_i\right] d\Omega + \int_{\partial\Omega}\left[-k \bullet \nabla M_i \bullet \hat{n} \bullet N_j\right] d\Gamma \bullet G_i = \int_{\Omega} f \bullet N_j d\Omega \tag{7}$$

Taking into account the directional derivative to consider the boundary conditions in the direction normal to the boundary, Eq. (7) can be expressed as shown in Eq. (8).

$$\int_{\Omega}\left[\rho \bullet C_p \bullet M_i \bullet \frac{\partial G_i}{\partial t}\right] \bullet N_j d\Omega + \int_{\Omega}\left[k \bullet \left(\nabla M_i \bullet \nabla N_j\right) \bullet G_i\right] d\Omega + \int_{\partial\Omega}\left[-k \bullet \frac{\partial M_i}{\partial \hat{n}} \bullet N_j\right] d\Gamma \bullet G_i = \int_{\Omega} f \bullet N_j d\Omega \tag{8}$$

Thus, the detailed Eq. (8) is the PDE to be solved by the model to obtain the temperature distribution $T = T(\{u\}, t)$ for every position $\{u\}$ and time instant t. In the source term f in Eq. (8) both the energy introduced by the laser, f_{laser}, and convection and radiation losses, f_{losses}, are included as indicated in Eq. (9). Their values are defined in section 3.6, where the f_{laser} is differentiated for the LM and GM.

$$f(\{u\}, t) = f_{laser}(\{u\}, t) + f_{losses}(\{u\}, t) \tag{9}$$

3.3. Basis of the mechanical model

The mechanical model is solved only in the GM by applying the material theory of elasticity, where the material is assumed to be in its elastic regime. With this theory, the relation between the applied forces, which in this case is the distortion caused by the laser heat input, and the resulting deformation is solved. Hooke's law is implemented to relate the strain and stress, Eq. (10), where $\{\sigma(\{u\})\}$ is the stress vector at a given position, $[D]$ is the elasticity matrix, and $\{\varepsilon(\{u\})\}$ is the deformation vector.

$$\{\sigma(\{u\})\} = [D] \bullet \{\varepsilon(\{u\})\} \tag{10}$$

Applying the elasticity theory, Eq. (11), the deformation $\{\varepsilon(\{u\})\}$ is given by the partial derivate of the displacements $\{\delta(\{u\})\}$, where the displacement on any point of the domain Ω is defined by the interpolation function $[N(\{u\})]$ and the nodal displacement $\{\delta\}$.

$$\{\varepsilon(\{u\})\} = [\partial] \bullet \{\delta(\{u\})\} = [\partial] \bullet [N(\{u\})] \bullet \{\delta\} \tag{11}$$

The mechanical model aims to determine the resulting displacements generated by the thermal nature of the LBW process, material expansion/contraction, and consequently the model is static. The nodal displacements introduced into the system, Eq. (12), are defined by means of the material coefficient of thermal expansion, CTE, and the temperature difference between the initial temperature of the part, T_{ini}, and the fusion temperature of the material, T_{fus}.

$$\{\delta\} = \int_{T_{fus}}^{T_{ini}} CTE \bullet \{T\} dT = CTE \bullet \{\Delta T\} \tag{12}$$

By substituting Eq. (11) in Eq. (10), and the resulting in Eq. (9), the obtained Eq. (13) represents the resultant equation to be solved in the PDE toolbox of Matlab, where a constant CTE coefficient is considered.

$$\{\sigma(\{x\})\} = [D][\partial][N(\{x\})]\{\delta\} = CTE[D][\partial][N(\{x\})]\{\Delta T\} \tag{13}$$

3.4. Weld path definition

The user determines the trajectory of the laser beam by introducing the most representative points of the weld path, and the model automatically unites these points with straight lines creating a continuous path. This path is subsequently discretised in small segments, Δu. When defining the trajectory matrix, $[TR]$, not only the welding head coordinates are introduced $[\{x\}\{y\}\{z\}]$, but also the laser power, $\{P\}$, and the welding speed, $\{F\}$.

$$[TR] = [\{x\}\{y\}\{z\}\{P\}\{F\}] \tag{14}$$

Overall, the trajectory is deployed in matrix form to achieve a reasonable resemblance to a CNC program. Therefore, the laser is automatically switched off when the laser power in the trajectory matrix changes from a positive value to null, and vice versa.

3.5. Initial conditions

The initial temperature of the workpiece, T_0, is set to 25 °C at every position $\{u\} = \{x, y, z\}$ of the whole domain Ω at the initial instant t = 0, Eq. (15). This temperature value has been measured experimentally before the tests. Once the model is initialized, the initial temperature of the following steps is defined by the temperature field obtained in the previous step.

$$\{T_0(\{u\}, 0)\} = 25 \ ^{\circ}\mathrm{C} \tag{15}$$

3.6. Boundary conditions

Three different boundary conditions, BC, are defined in the domain Ω, see Fig. 2. The first one is the area irradiated by the laser beam, Γ_1. The laser beam is modelled as a heat source, $f_{laser}(\{u\}, t)$, but its distribution varies depending on the LM or GM, Eq. (16) and (17), respectively. The second BC, Γ_2, corresponds to all the external faces. The third and last BC is established at the contact area of the fixed support, Γ_3, which is situated on the left side of the plate in Fig. 2.

The employed fibre laser has a top-hat transversal energy distribution, and therefore, in the LM the laser beam is shaped as a moving top-hat heat source, Eq. (16), where α is the welding mechanism dependent absorptivity, $P(t)$ is the time-dependent laser power, R is the laser beam radius, $d(\{u\})$ the laser defocus distance at a $\{u\}$ position, and φ is the laser beam divergence angle. The area Γ_1 where the laser beam is focused in the LM is represented in Fig. 3. Note that the value of the heat source, $f_{laser}(\{u\}, t)$, is updated in every time step of the LM as the laser beam position, $\{u\}$, varies. Time step values employed for the LM simulations are given in Table 1.

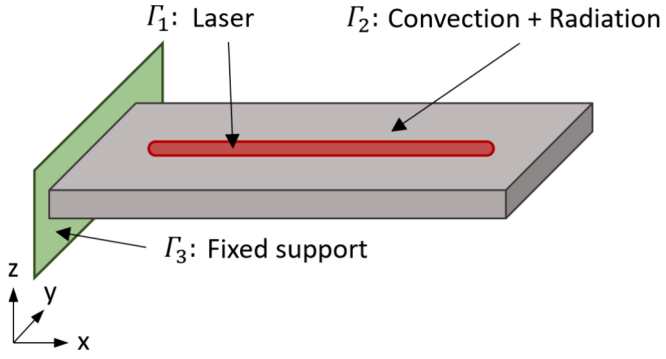

Fig. 2. Boundary conditions for the GM.

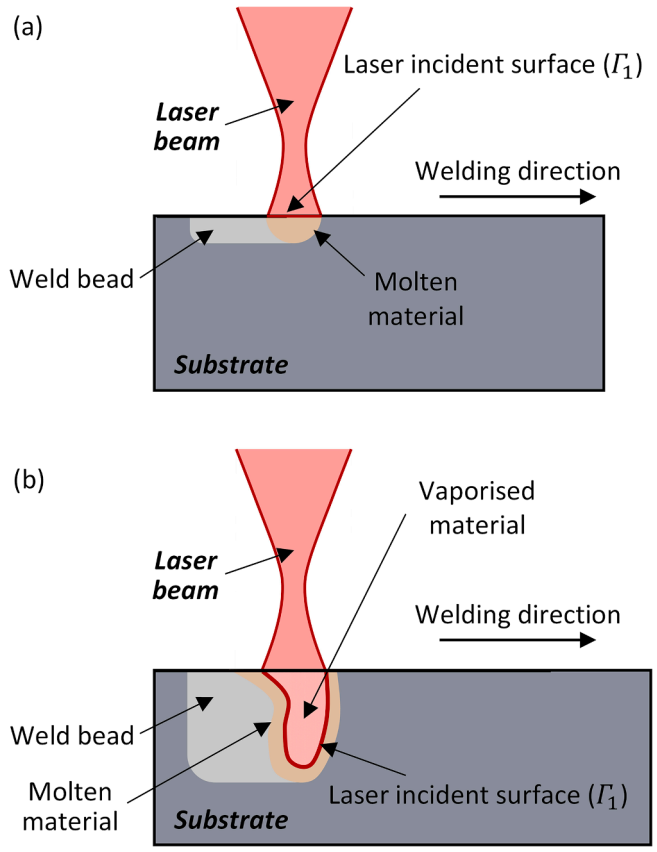

Fig. 3. Surface where the laser heat is introduced depending on the welding mode in the LM: (a) Conduction welding and (b) Keyhole welding.

Table 1
Main parameters for the numerical simulations.

Parameter	Value		Units
	LM	GM	
Element size (max, min)	(1, 0.2)	(2, 0.2)	[mm]
Trajectory discretization step,Δu	0.05–0.1	0.1–0.2	[mm]
Time step, t	0.012–0.024	2.7–10.8	[s]
Absorptivity,α	0.4–1		[-]
Mesh growth rate, r	1.1		[-]
Laser beam divergence angle,φ	6.18		[°]
Laser radius,R	0.5–1.0		[mm]
Convection coefficient, h_c [36]	10		[W·m^{-1}·K^{-1}]
Radiative emittance,ε	0.4		[-]
Room temperature,T_{room}	25		[°C]
Fusion temperature,T_{fus}	1350		[°C]
Vaporisation temperature,T_{vap}	3100		[°C]

$$f_{laser}(\{u\},t) = \frac{\alpha \bullet P(t)}{\pi \bullet (R + d(\{u\}) \bullet tg(\varphi))^2} \in \Gamma_1 \tag{16}$$

Depending on the welding mechanism the absorptivity varies, and also the laser incident surface, see Fig. 3. In conduction welding, the laser is introduced on the upper surface of the plate, Fig. 3(a), whereas once the vaporisation temperature, T_{vap}, is exceeded those elements are eliminated and the laser penetrates the substrate, Fig. 3(b). In keyhole welding, the laser reflections are simulated by introducing the beam on the surface between the vaporised and the liquid material and increasing the absorptivity up to the unit value.

In the GM, the weld bead is simulated in an integer number of steps, one step per weld bead in the present study, where the laser irradiates the corresponding bead section in each step. In Table 1 the corresponding time steps are indicated. The GM introduces the same amount of energy as the experimental welding, but at a lower computational cost as the number of steps is reduced considerably. Contrary to the LM, in the GM the employed $f_{laser}(\{u\},t)$ heat source has a rectangular shape which length is determined by the length of the weld bead and the width is obtained from the LM. For this purpose, multiple melt pool geometries obtained in the LM are overlapped in every trajectory discretization step,Δu. The energy density of the laser in the GM is distributed homogeneously along the weld bead area, A, as represented in Eq. (17), where t_1 and t_2 are the initial and final times of the weld step, respectively, α is the welding mechanism dependent absorptivity, and $P(t)$ is the time-dependent laser power.

$$f_{laser}(\{u\},t) = \frac{\alpha \int_{t_1}^{t_2} P(t)dt}{A} \in \Gamma_1 \tag{17}$$

The second BC represents the convection and radiation heat losses and is applied to all external faces except the one in contact with the clamping tool. These losses are displayed in Eq. (18), where h_c is the convection coefficient, ε is the radiative emittance, and σ is the Stefan-Boltzmann constant (5.67×10^8 W·m^{-2}·K^{-4}). The air convection coefficient is typically between 5–25 W·m^{-1}·K^{-1} and in the present work a constant value of 10 W·m^{-1}·K^{-1} is considered as did Heigel et al. [36]. Besides, the material emissivity is defined based on Kirchhoff's law of thermal radiation which states that the emissivity and absorptivity take the same value. Specific data is provided in Table 1.

$$f_{losses}(\{u\},t) = -h_c \bullet (T(\{u\},t) - T_{room}) - \varepsilon \bullet \sigma \bullet \left(T(\{u\},t)^4 - T_{room}{}^4\right) \in \Gamma_2 \tag{18}$$

The third and last BC represents the contact between the clamping tool and the metal plate. The clamping tool is assumed to maintain its temperature during the welding process due to its large size and high thermal inertia. Therefore, this external face is assumed to have a constant room temperature, as shown in Eq. (19).

$$\{T(\{u\},t)\} = T_{room} \in \Gamma_3 \tag{19}$$

For the mechanical model resolution in the GM, the only BC is the zero-displacement condition imposed in the clamping face.

$$\{\delta(\{u\},t)\} = \{0\} \in \Gamma_3 \tag{20}$$

3.7. Mesh generation

In Fig. 4 the mesh employed in the GM and LM are shown, where the LM is extracted at the weld bead centre. Due to the high thermal gradient in LBW, the mesh in the regions close to the weld bead and the heat-affected zone is refined. First-order tetrahedral elements have been used due to their good adaptability to complex geometries. The maximum and minimum element sizes used are listed in Table 1 together with the main parameters for the numerical simulations. Note that in each simulation the independence of the results regarding the employed element size and time step is ensured through the corresponding study as shown in section 7.2.1.

The mesh generation starts by meshing the whole part with

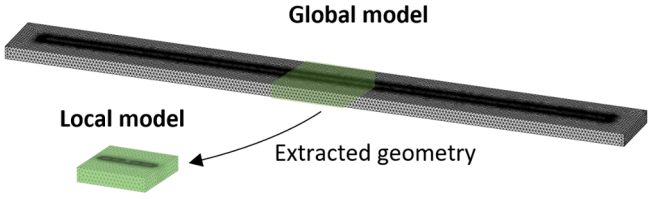

Fig. 4. Mesh implemented in the simulations for the local and global models.

minimum size elements. Afterwards, in a second step the size of the elements further from the laser path is increased according to the mesh growth rate, which allows to reduce the computation cost associated to the problem resolution. The mesh generation code is provided in Appendix A.

4. Material and equipment

The LBW validation tests are carried out on 10 × 100 × 2 mm Inconel 718 plates supplied by Haynes International with the chemical composition listed in Table 2. The geometry for the GM is equal to the whole plate. However, for the LM a smaller 10 × 10 × 2 mm part size is employed, see Fig. 4. The size ratio between the LM geometry and the whole part is 1/10 which is proven to give positive results for thermal models [37]. Xu et al. experimentally validated that ratios above 3/50 between the model size and the whole part provide a reasonable accuracy.

The thermophysical properties of Inconel 718 are implemented as temperature-dependent in the model, Table 3, and their values are linearly extrapolated when higher temperatures are obtained. On the contrary, as the mechanical model is static, mechanical properties are considered constant: 200 GPa elastic modulus and a 14 $\mu m \cdot m^{-1} \cdot K^{-1}$ CTE value [38].

In the experimental tests, a fibre laser from Coherent-Rofin with a maximum power of 1 kW in CW is employed. The laser beam has a 1070 nm wavelength and is delivered by a fibre system to the welding head where a 200 mm focusing optic is used. The welding head is mounted on a five-axis laser centre and an Argon 2X protective gas with 99.99 purity supplied by Nippon Gases is used in the upper and lower faces of the plates.

5. Monitoring system

An in-situ monitoring system is implemented based on a two-colour pyrometer, a CMOS coaxial camera, and a height sensor, see Fig. 5. The data provided by the monitoring systems is simultaneously extracted from the process.

The employed IGAR 12-LO pyrometer has a measuring temperature range between 500–2500 °C with an acquisition frequency of 60 Hz. In order to avoid overloads during the keyhole welding, the pyrometer is mounted off-axis and placed 2 mm into the tail of the weld, where it is focused in an area of 1 mm diameter on the surface of the plate. The same configuration is employed in all tests and the positioning of the pyrometer is ensured through the coaxial camera.

As regard to the camera-based vision sensing, a VIS/NIR imaging camera is selected to capture the melt pool geometry, see Fig. 5, as well as guarantee the pyrometer positioning. The camera is a CS135MUN from Thorlabs, which has a 1.3MP resolution equivalent to 1280 × 1024 pixels and a NIR enhanced CMOS sensor with a 150-fps acquisition rate. The camera is connected to a PC through USB3.0 and the images obtained are processed in Matlab R2023a, with a 79 $pixel \cdot mm^{-1}$ accuracy.

The height sensor is employed to measure the vertical displacement of the plate before and after the welding process. For that matter, the HG-C 1200-P micro laser distance sensor of the CMOS type is selected. The height sensor has an approximate 300 μm diameter and a measurement centre located at a 200 mm distance with a ± 80 mm measuring range and a 200 μm repeatability. The sensor has a response time of 1.5 ms, which is equal to an acquisition frequency of 666.67 Hz.

Table 3
Thermophysical properties of Inconel 718; density (ρ), specific heat (C_p), and conductivity (k) depending on the temperature (T) [39].

T [K]	ρ [kg•m^{-3}]	C_p [J•kg^{-1}•K^{-1}]	k [W•m^{-1}•K^{-1}]
298	8190	435	8.9
373	8160	455	10.8
473	8118	479	12.9
573	8079	497	15.2
673	8040	515	17.4
773	8001	527	18.7
873	7962	558	20.8
973	7925	568	21.9
1073	7884	585	23.9
1173	7845	603	25.8
1273	7806	620	26.7
1373	7767	640	28.3
1443	7727	650	29.3
1609	7400	720	29.6

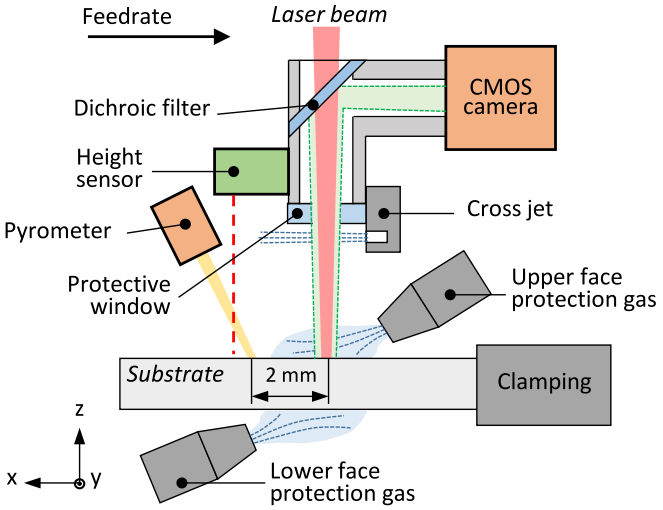

Fig. 5. Experimental set-up and employed monitoring system.

6. Experimental tests

For the experimental tests, the butt-welding strategy is selected. A suitable tool is designed to clamp the plate and ensure a strong joint and avoid undesirable deformation. For the initial tests, samples 1–25 detailed in Table 4, the LBW is applied to a single Inconel 718 plate in order to avoid possible misalignment errors or the influence of the edge preparation in the experimental tests. Afterwards, in the case study detailed in section 7.3 two individual plates are butt-welded both experimentally and digitally.

In the LBW tests, three parameters are considered: the laser beam radius (R), the laser power (P), and the laser feed rate (F), which are employed to determine the power density (PD) and the laser-material interaction time (IT) as indicated in Eq. (21) and Eq. (22), respectively.

$$PD = \frac{P}{\pi \bullet R^2} \tag{21}$$

$$IT = \frac{2 \bullet R}{F} \tag{22}$$

Table 2
Chemical composition of the as-received Inconel 718 (wt. %).

Ni	Co	Fe	Cr	Nb + Ta	Mo	Mn	Si	Ti	Al	C	B
Bal.	<1.000	19.000	18.000	5.000	3.000	<0.350	<0.350	0.900	0.500	0.050	0.004

Table 4
All the parameter combinations for the experimental tests.

Sample	*P (W)*	*F (mm·min^{-1})*	*R* (mm)	*PD* (W·mm^{-2})	*IT* (ms)
1	1000	1000	0.5	1273.240	60
2	800	1000	0.5	1018.592	60
3	600	1000	0.5	763.944	60
4	400	1000	0.5	509.296	60
5	200	1000	0.5	254.648	60
6	1000	1000	1.0	318.310	120
7	800	1000	1.0	254.648	120
8	600	1000	1.0	190.986	120
9	400	1000	1.0	127.324	120
10	200	1000	1.0	63.662	120
11	1000	2000	1.0	318.310	60
12	800	2000	1.0	254.648	60
13	600	2000	1.0	190.986	60
14	400	2000	1.0	127.324	60
15	200	2000	1.0	63.662	60
16	1000	500	0.5	1273.240	120
17	800	500	0.5	1018.592	120
18	600	500	0.5	763.944	120
19	400	500	0.5	509.296	120
20	200	500	0.5	254.648	120
21	1000	2000	1.0	1273.240	30
22	800	2000	1.0	1018.592	30
23	600	2000	1.0	763.944	30
24	400	2000	1.0	509.296	30
25	200	2000	1.0	254.648	30

During the experimental tests, the height displacement of the plate is measured in situ, in order to obtain a comparable result to validate the mechanical model. For the ex-situ monitoring, the 25 weld beads were metallography inspected by cross-sectioning three samples in each bead, located at a 1/10, 5/10, and 9/10 of the bead length. Through an automatic polisher from Metkon, the FOCIMAT 52 automatic head mounted in a FORCIPOL 102 polisher, the metallographic procedure for nickel-based alloys recommended by the manufacturer is applied for the sample grinding and polishing. Afterwards, the microstructure is revealed using Kalling 2 etching agent. Finally, the metallography is analysed in a Leica DCM-3D optical microscope.

7. Results and discussion

For the validation of the LBW model, first, the experimental results are inspected. Thus, the most significant samples are selected to validate the model, and the different welding regimens registered during the joining process are verified. Therefore, this section is divided into two parts: one for the experimental results, and another one for the model validation.

7.1. Experimental results

The analysis of the experimental results show three welding regimes, where the PD applied to the welding area is confirmed to be the most significant parameter. The limits between the different regimes are defined by the PD [36] and the depth/width aspect ratio of the bead [40], where values around 10^3 W·mm^{-2} and 0.5 are defined, respectively, as the boundaries between the conduction and keyhole-welding modes. Nevertheless, this boundary is blurry, and the third regime is defined as the mixed-mode, which represents the transition between conduction and keyhole. In Fig. 6 the identified three welding regimens are shown.

For instance, in the following graph (Fig. 7) the weld aspect ratio and PD values corresponding to samples 21 to 25 are shown. The red area of the graph represents the keyhole region where the aspect ratio and the PD are above 0.5 and 10^3 W·mm^{-2}, respectively. Besides, the orange area indicates the conduction welding region, thereby in the rest of the graph the mixed-mode welding happens. The error bar represents the deviation encountered in the three sections analysed. As it can be seen, conduction welding is a much more stable welding regime, which goes in line with the statement indicated by the assumptions that a stable welding regime implies a constant behaviour of the melt pool dynamics [16].

By means of the coaxial camera depicted in Fig. 5 the reflections of the melt pool were recorded in the visible and NIR wavelengths. Afterwards, a filtering code is applied in Matlab to the recorded images [41] and a remarkable difference between the LBW modes is obtained as shown in Fig. 8. On the one hand, the high reflections of the keyhole welding are represented in the first non-corrected picture. For the conduction case, the melt pool is more stable, and no plasma plume appears. On the other hand, the CNC-programmed laser radius is well represented in the coaxially monitored data, where the conduction and keyhole welding bead stages show a good correlation with the laser radius of 1

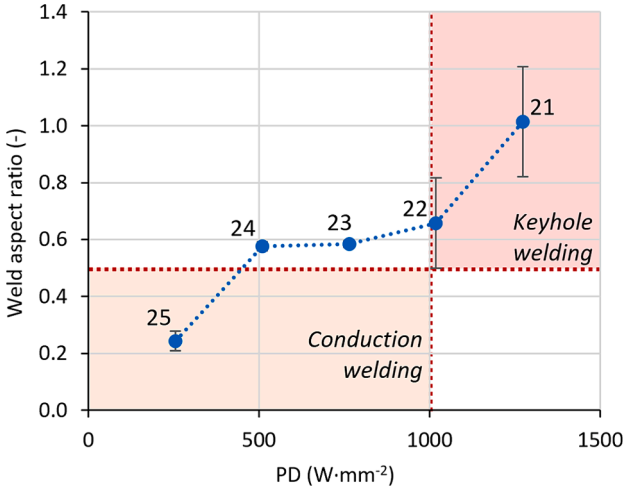

Fig. 7. LBW mode determination based on the weld aspect ratio and the PD for samples 21–25.

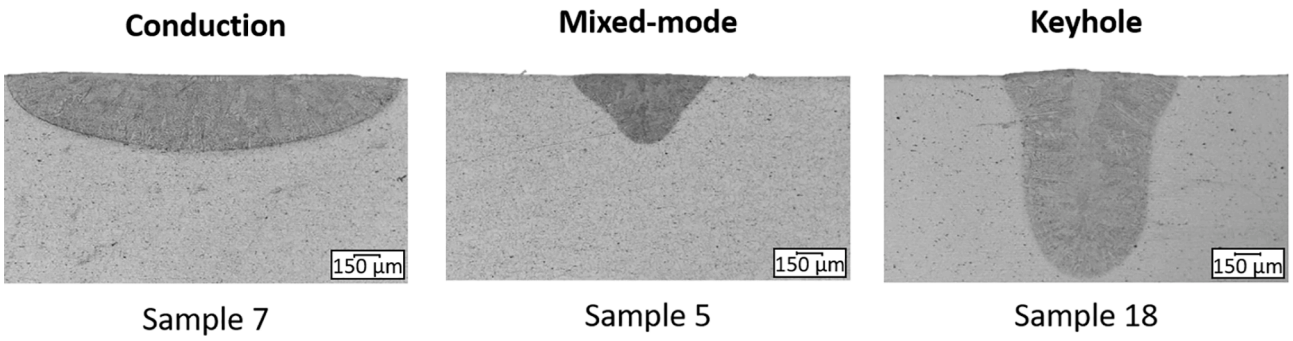

Fig. 6. Identification of the three welding regimes.

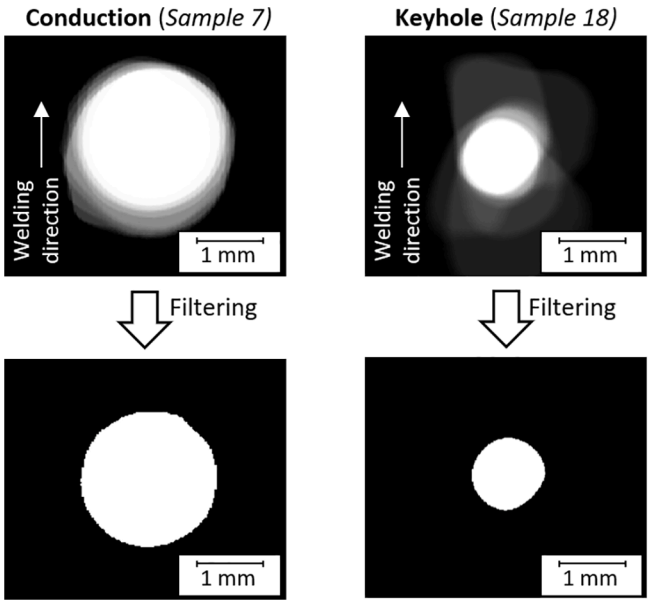

Fig. 8. Coaxial camera results for different LBW mechanisms: the non-corrected image obtained after averaging 10 frames (0.067 s) and the filtered image for determining the melt pool size.

mm for conduction and of 0.5 mm for keyhole welding.

Regarding the influence of the process parameters: the PD, the laser-material IT, and the laser spot radius were confirmed to be the most significant for the LBW process, see Fig. 9. Therefore, with regard to the main welding parameters, the following statements are extracted:

- The weld depth depends mostly on the PD and shows a linear increasing relation. Even though the IT also presents a linear increasing relation with the penetration, the slope of this second is less pronounced.
- The weld bead width inevitably changes in accordance with the laser radius. The laser spot size affects the PD and the IT. Nonetheless, the IT has a major influence on the weld bead width.
- The welding regime depends mostly on the PD. However, the IT also has a relevant influence.

Regarding the displacements measured during the welding process, they revealed that the deformation depends mainly on the heat-affected zone. For instance, in the case of conduction welding the plate presents a more significant deformation, as it was meant to achieve. In Fig. 10 the Z-axis deformation of the welded plates is represented, where sample 2 is a keyhole welding and sample 7 is a conduction welding.

The welding parameters that influence the process have been identified through experimental testing. Hence, in future welds, the starting parameters will be easier to spot. For instance, if a deeper weld is desired, the PD will be the main parameter to be increased. Furthermore, this approach is directly applied in the development of the model, as the prediction capability of the model is built up on process knowledge.

7.2. Validation of the numerical model

The LBW model validation consists of two steps. On the one hand, the validation of the local model (LM), where the melt pool temperature and the weld bead dimensions are evaluated. And, on the other hand, the validation of the global model (GM) where the plate deformation is quantified. However, the first step of the validation is to study the grid independence.

In order to validate the numerical model under the most representative conditions, the six different weld beads listed in Table 5 were

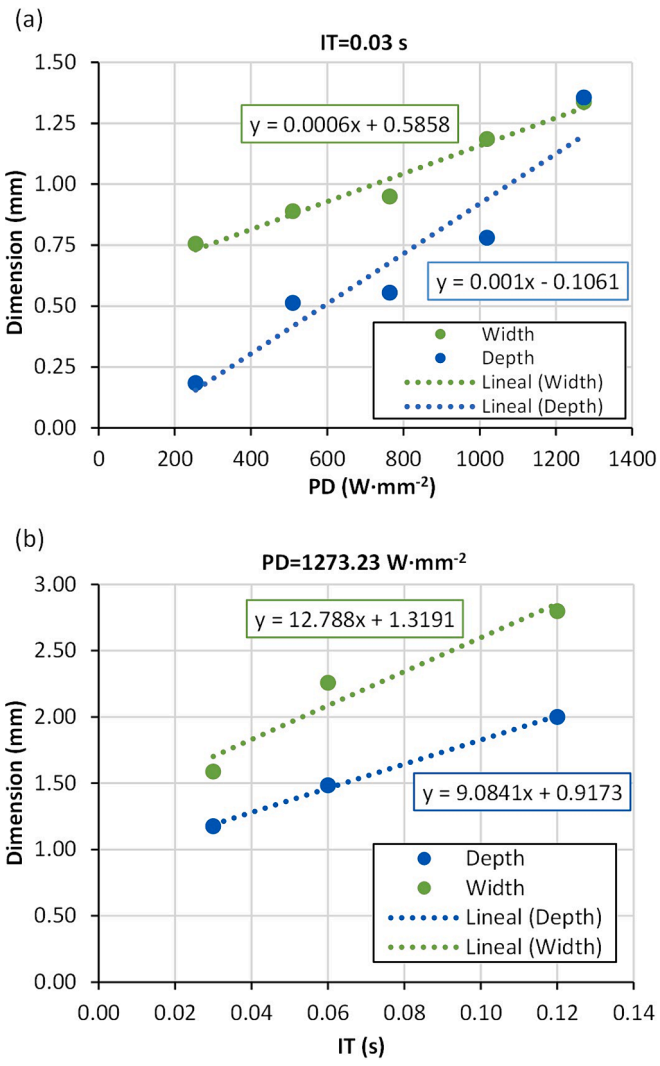

Fig. 9. Summary of the influence of LBW parameters on the weld bead depth and width when: (a) Increasing the power density and (b) Increasing the interaction time. Each individual data represents the average dimension of the three cross-sections analysed.

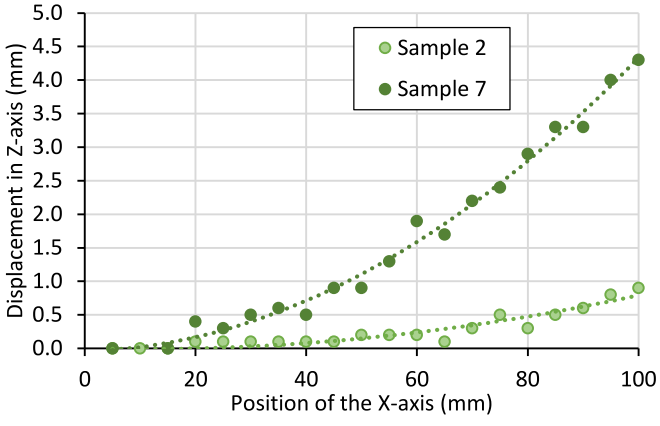

Fig. 10. The Z-axis deformation of the welded plates.

Table 5
Summary of the samples implemented for the model validation.

Sample	*PD* (W·mm^{-2})	*IT* (ms)	*R* (mm)
2	1018.592	60	0.5
5	254.648	60	0.5
7	254.648	120	1.0
10	63.662	120	1.0
12	254.648	60	1.0
18	763.944	120	0.5

selected, since they represent all the possible welding regimes. Detailed simulation data for each sample is provided in Appendix B.

7.2.1. Grid independency study

Before simulating the different scenarios, a grid independence study was performed to define the element size that provides mesh-independent results and the optimum element size that enables accurate results but at a reasonable cost.

During the grid independency study the process temperatures and weld bead dimensions were evaluated. For instance, in Table 6 the weld bead temperature, width, and depth results of the LM for sample 12 are shown for a varying minimum element size. It can be seen how element sizes below 0.2 mm barely reduce the numerical error but drive up the calculation time. On the contrary, increasing the minimum element size from 0.2 to 0.3 mm hardly has any effect on the calculation time, but the width and depth errors increase more than double. Regarding the temperatures, almost no variations are detected.

Overall, this study concludes that the minimum element size required for the LBW simulations is 0.2 mm. Moreover, this result is consistent with the work presented by Luo et al., who recommend that the optimum mesh for LBW should cover the laser heat source with at least 4 elements to obtain reliable results [42]. By applying this recommendation to the model, a minimum element of 0.25 mm or less should be used, hence 0.2 mm is considered adequate.

7.2.2. Local model validation

7.2.2.1. Temperature during the LBW process. The melt pool temperature obtained at the LM is validated through the in-situ monitoring with the pyrometer. Taking into consideration the pyrometer characteristics, the maximum temperature is measured in an area of 1 mm diameter positioned 2 mm behind the melt pool, see Fig. 5. Therefore, the pyrometer and LM temperatures, $T_{pyrometer}$ and T_{LM} respectively, shown in Table 7 correspond to the average values measured at that position during the whole welding test.

The LM temperatures show a little error being the maximum of 157.75 °C, which is an acceptable deviation in accordance with other authors [43,44]. The maximum error appears in the tests corresponding to the keyhole welding. However, its value is assumed as acceptable considering that the melt pool dynamics have been neglected to reduce the computational cost of the model.

In Fig. 11 the thermal results of sample 10 are summarised. The full thermal field of the LM is shown in Fig. 11(a), whereas, the YZ and XZ cross sections of the weld bead are shown in Fig. 11 (b) and (c), respectively.

Table 7
The experimental and LM average temperatures, $T_{Pyrometer}$ and T_{LM}, respectively.

Sample	$T_{Pyrometer}$ (°C)	T_{LM} (°C)	Error (°C)
2	1471.62	1629.37	157.75
5	698.26	701.93	3.67
7	1853.15	1887.21	34.06
10	1045.36	1049.27	3.91
12	1785.96	1756.79	29.17
18	1443.15	1585.30	142.15

7.2.2.2. Weld bead dimensions. The weld bead width and depth have been measured by metallographic inspection to define their dimensions experimentally. Three cross-sections have been studied and averaged for each sample. The modelled dimensions are calculated according to the melt pool limit defined by the fusion temperature, T_{fus}, as shown in Fig. 12. All the weld bead depth and width values from the LM and experimental samples are collected in Table 8.

The results confirm that the error in the weld bead dimensions varies from 50 μm to 450 μm. Fig. 13 shows the numerical results of the modelled depth and width compared with the experimental values with the respective deviation error bars.

Overall, higher errors are obtained for the keyhole welding tests, like sample 18, as no melt pool dynamics are considered to reduce the computational cost. Two examples with different welding modes are displayed in Fig. 14, in which the red line represents the model results superimposed on the bead cross-section.

The deviation between the experimental and modelled results is mostly due to the assumptions made in the development of the numerical model. Neglecting the melt pool dynamics and considering a constant material absorptivity are considered as the main reasons for the obtained disparities when comparing experimental and modelled results.

On the one hand, the melt pool dynamics have a direct influence on the geometry of the weld bead, as they promote the heat transfer within the melt pool through convection, as well as conduction. Hence, depending on the material currents, slightly different cross-section shapes are obtained. However, if they are omitted the only heat transfer mechanism within the melt pool is conduction and this produces a shape error to be quantified.

On the other hand, the absorptivity of the material controls the amount of heat introduced into the welding process. Therefore, variations of the real absorptivity due to its dependence on the material temperature or the surface finish that are not considered in the model can lead to weld bead size errors. However, the obtained errors in Table 8 are considered acceptable considering the low computational cost of the model and the need to balance accurate results and fast simulation times.

7.2.3. Global model validation

7.2.3.1. Displacement in Z-axis. The mechanical problem solved in the GM is validated by means of the vertical displacement caused by the material contraction after the LBW process. The displacements achieved in the GM and the experimental results are listed in Table 9 along with the respective error. In Fig. 15 the developed thermal field in the GM at

Table 6
Test 12 weld bead results of the model, M, for the grid independency study compared with the experimental tests, Exp.

Minimumelement size	Temperature (°C)			Width (mm)			Depth (mm)			Time (s)
	Exp.	**M**	**Error**	**Exp.**	**M**	**Error**	**Exp.**	**M**	**Error**	
0.1	1785.96	1781.44	4.52	1.93	1.98	0.05	0.30	0.33	0.03	59322.00
0.2	1785.96	1784.50	1.46	1.93	1.80	0.13	0.30	0.33	0.03	1295.40
0.3	1785.96	1790.76	4.80	1.93	1.50	0.43	0.23	0.33	0.11	1044.00

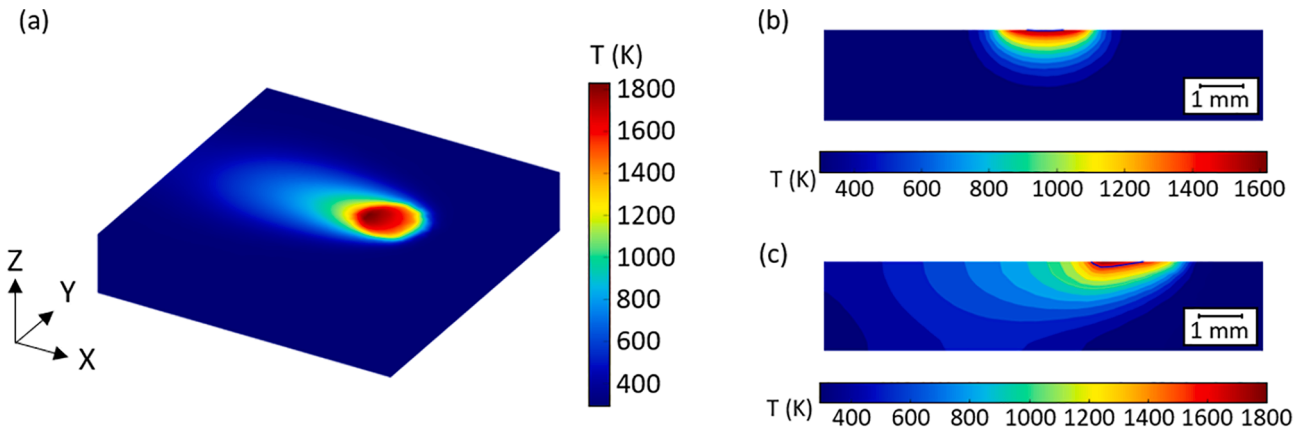

Fig. 11. LM temperature field of sample 10: (a) 3D view of the LM thermal results, (b) Cross section in YZ plane at the laser centre and (c) Cross section in XZ plane.

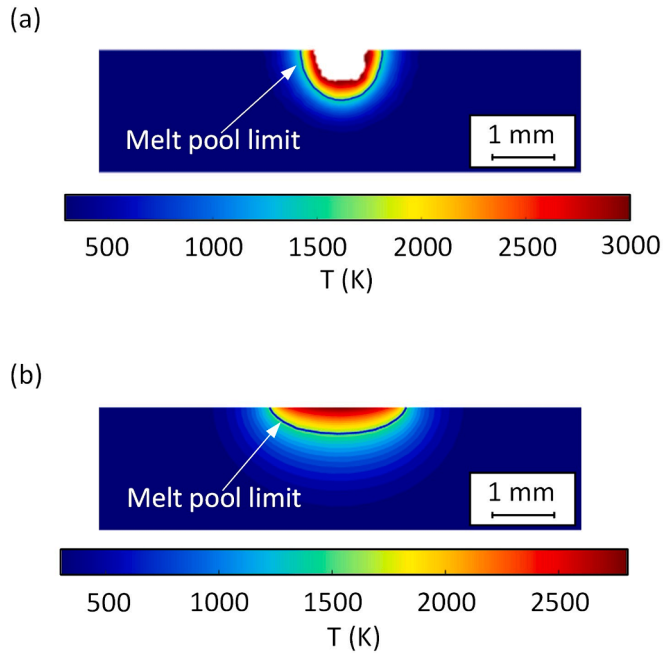

Fig. 12. Temperature field in the LM: (a) Sample 2 and (b) Sample 7.

Table 8
The experimental, Exp., and LM results of the weld bead dimensions, depth and width, and the corresponding welding mode for each sample.

Sample	Depth (mm)			Width (mm)			LBW mode
	Exp.	LM	Error	Exp.	LM	Error	
2	1.15	0.96	0.19	1.58	1.56	0.02	Keyhole
5	0.44	0.34	0.10	0.89	0.79	0.10	Mixed-mode
7	0.53	0.54	0.01	2.49	2.13	0.36	Conduction
10	0.12	0.13	0.01	0.89	0.94	0.05	Conduction
12	0.33	0.25	0.08	2.02	1.93	0.09	Conduction
18	1.28	0.84	0.44	1.11	1.56	0.45	Keyhole

the final welding time instant for sample 12 and the resulting vertical displacement due to the material shrinkage are depicted.

With an average error of around 150 μm, the small difference between the experimental results and the displacements obtained with the GM is noteworthy. Based on the obtained results, it can be concluded that simulating the whole weld bead at once and calculating the resulting material shrinkage is an appropriate procedure because it enables the simulation of relatively big parts at a low computational cost. It should be noted that for this step the dimensions of the weld bead are required, which are extracted from the LM.

7.3. Validation of the model for dissimilar plate welding: Case study

Finally, the suitability of LBW model is tested with a real butt welding of two equal plates of size 10 × 100 × 2 mm. The welding is performed along the longest side of the plates in order to maintain similarity with the previous tests. The parameters implemented in this case study are equal to the parameters of sample 2 (see Table 4).

As in the previous experimental test, the temperature readings are taken 2 mm back from the melt pool. With the individual measurements, the mean temperatures are calculated and in the experimental measurement a 1400 °C average temperature is obtained, compared to the 1651 °C predicted by the model.

The temperature results show a higher error, 253.47 °C, than in the validation tests presented in Section 7.2. This higher error in the case study is attributed to the fact that the model does not include the gap between the welded plates. Despite edge preparation, it is not possible to ensure a perfect positioning, and this increases the error of the model. Consequently, improper edge preparation and the presence of gaps or misalignments between the plates would increase the error of the model.

The modelled weld bead presents a 1.28 mm depth and a 1.64 mm width, compared to the 1.36 mm depth and 1.36 mm width experimentally measured. Overall, a weld bead dimensional error below 100 μm is considered satisfactory. Fig. 16(a) displays the dimensional difference of the width and depth for the given case study. Moreover, in Fig. 16(b) and (c) the thermal fields of the LM and GM are displayed, respectively.

As it can be seen in Fig. 16(a), in the experimental welding test a small separation of the plates is detected. In the developed model, the plate deformation is calculated in the GM and although it shows that tensile stresses are generated in this area, the LM does not consider plate separation in the current stage of the model. Consequently, if the fixing system used is inappropriate and allows plate separation during the welding, the error of the model would increase.

8. Conclusions

In view of the need for predictive models for laser processes, particularly LBW, a thermomechanical model of the LBW process is developed. The novelty of the research lies in the use of a multiscale approach in which the laser heat source automatically adapts to the welding regime. This ensures a computationally efficient numerical model, without the need to consider the melt pool dynamics. The numerical model has been validated through experimental tests for different LBW conditions and a reasonable accuracy has been obtained

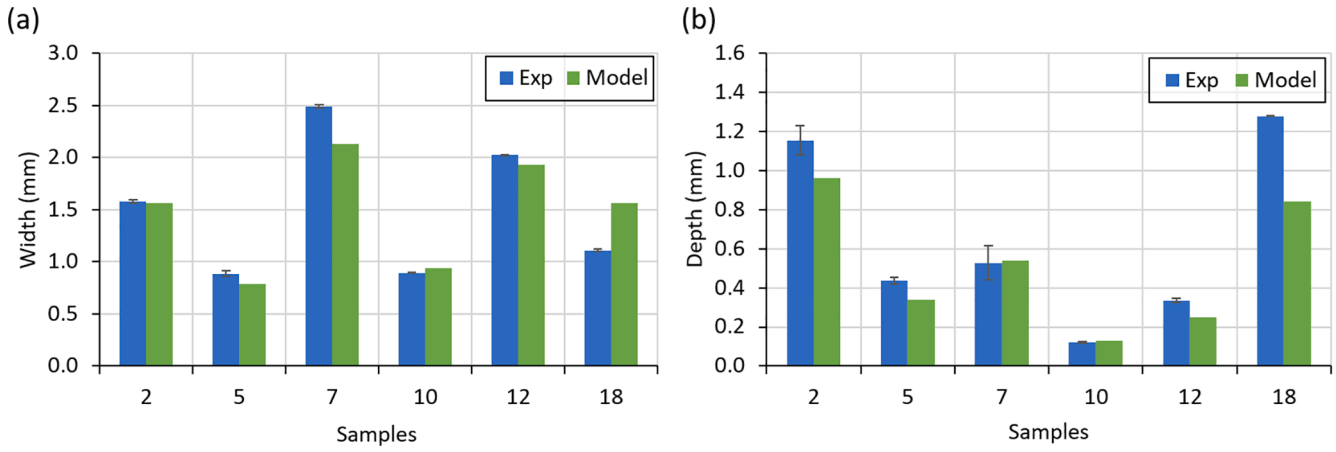

Fig. 13. Comparison of the modelled and experimental results with their respective error deviation bars: (a) width, and (b) depth.

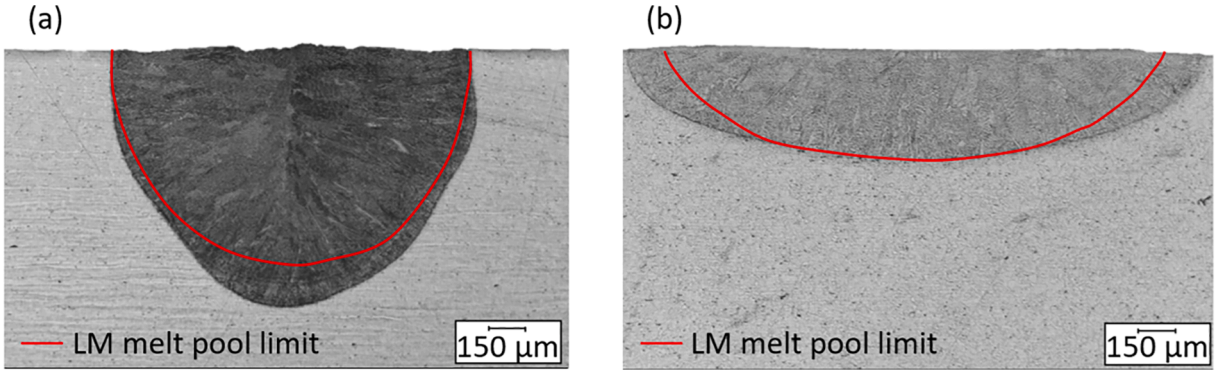

Fig. 14. Correlation between the modelled weld bead dimensions and the metallography: (a) Sample 2 and (b) Sample 7.

Table 9
The experimental and modelled values of the resultant maximum Z-axis displacement.

Sample	Exp. (mm)	Model (mm)	Error (mm)
2	0.90	0.81	0.09
5	2.45	2.22	0.23
7	4.30	4.27	0.03
10	2.54	2.79	0.25
12	4.15	3.99	0.16
18	0.77	0.89	0.12

in all situations. The following are the main conclusions reached at the completion of the present research:

- The developed multiscale model based on a LM and a GM is capable of determining the welding regime and automatically adapts the heat transfer into the workpiece accordingly. Therefore, the user does not need to know the welding regime in advance and modify the heat source.
- It has been experimentally observed that the conduction welding is a more stable regime, and this facilitates the modelling of the process. On the contrary, the omission of the melt pool dynamics mainly affects to deep or keyhole welds, where a higher error is obtained.
- The mechanical problem solved in the GM shows an appropriate prediction of the vertical deformation of the welded plates. The model catches adequately the welding mechanism in the LM and the afterwards material shrinkage in the GM. Therefore, the multiscale approach is proven as a proper choice for the LBW modelling.

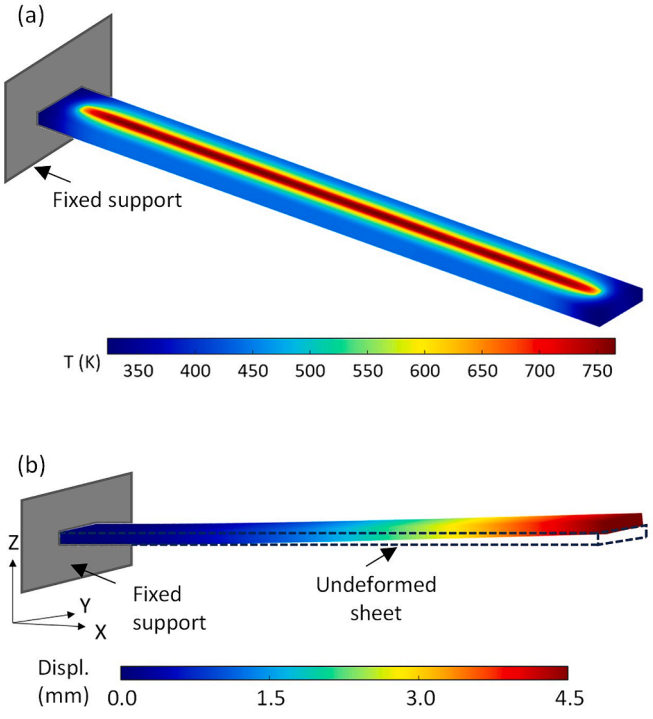

Fig. 15. (a) Temperature field of the GM for Sample 12 at the end time, simulation time 2.7 s, and (b) the corresponding Z-axis displacement once the plate is cooled down.

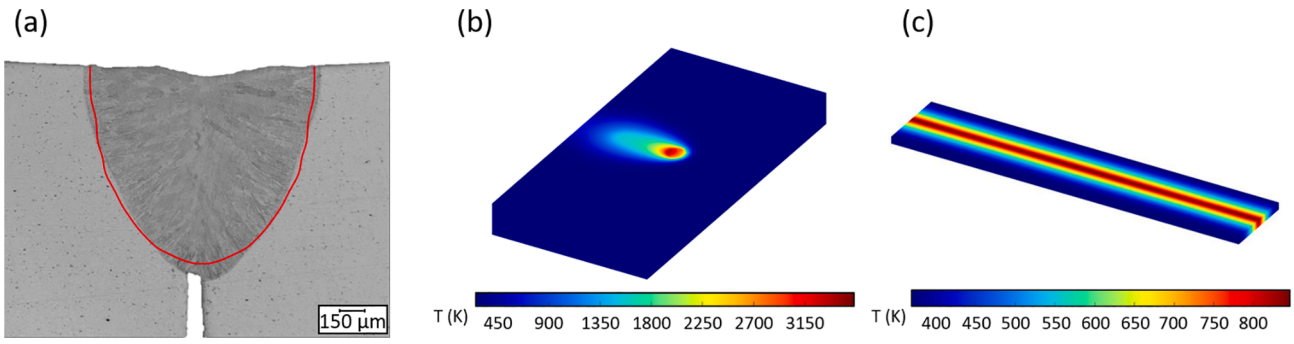

Fig. 16. Results of the case study: (a) Correlation between the modelled weld bead dimensions and the metallography for the case study; (b) LM melt pool temperature results; and (c) GM heat accumulation results.

- Upon reviewing the results of the experimental tests, the limit between the conductive and keyhole welding regimes is concluded to be mainly dependent on the PD. Nonetheless, there is a need of further study to establish a more defined boundary for the different welding modes.
- The butt welding of two equal plates demonstrates how the initial experimental tests are adequate to validate the LBW model. However, the obtained error depends on the employed fixing system and edge preparation. If the fixing system is not rigid enough or the plates are not properly positioned and prepared, the results of the model would differ from the experimental, as these phenomena are not considered in the model.

In the near future, the research will focus on the application of the LBW numerical model to more complex cases. For instance, the welding of plates with different thicknesses or non-linear welding paths. Besides, as the current model calculates the distortions after the welding process, there is still room for improvement to compensate automatically the distortions and to avoid collisions between the laser head and the part during the welding process.

CRediT authorship contribution statement

O. Murua: Writing – review & editing, Writing – original draft, Validation, Software, Methodology, Investigation, Formal analysis, Data curation, Conceptualization. **J.I. Arrizubieta:** Writing – review & editing, Writing – original draft, Supervision, Software, Resources, Methodology, Investigation, Funding acquisition, Formal analysis, Conceptualization. **A. Lamikiz:** Writing – review & editing, Supervision, Resources, Methodology, Formal analysis, Conceptualization. **H.I. Schneider:** Writing – review & editing, Supervision.

Declaration of competing interest

The authors declare the following financial interests/personal relationships which may be considered as potential competing interests: Jon Inaki Arrizubieta reports financial support was provided by Spain Ministry of Science and Innovation. If there are other authors, they declare that they have no known competing financial interests or personal relationships that could have appeared to influence the work reported in this paper.

Acknowledgements

Grant TED2021-130543B-I00 funded by MCIN/AEI/10.13039/501100011033 and by the European Union NextGenerationEU/PRTR.

Appendix A

The mesh generation code employed in Matlab is provided as supplementary material. Download the “geo_100x10x2.stl” geometry and the “LaserPath.txt” file and copy them to the same folder as the “Mesh_generation.m” code. Introduce the desired simulation parameters and run the program to obtain the resulting mesh.

Appendix B

In this section, the main parameters employed in the simulations, described in Table 1, are specified in detail for each case in the following Table B.1.

Table B.1
The main parameters employed in each simulation.

Sample	Laser radius, R [mm]	Time step, t [s]		Trajectory discretization step, Δu [mm]		Element size (max–min) [mm]		Growth rate [-]
		LM	GM	LM	GM	LM	GM	
2	0.5	0.012	5.4	0.05	0.1	1.0–0.2	2.0–0.2	1.1
5	0.5	0.012	5.4	0.05	0.1	1.0–0.2	2.0–0.2	1.1
7	1.0	0.024	5.4	0.1	0.2	1.0–0.2	2.0–0.4	1.1
10	1.0	0.024	5.4	0.1	0.2	1.0–0.2	2.0–0.4	1.1
12	1.0	0.012	2.7	0.1	0.2	1.0–0.2	2.0–0.4	1.1
18	0.5	0.024	10.8	0.05	0.1	1.0–0.2	2.0–0.2	1.1

Appendix C. Supplementary material

Supplementary data to this article can be found online at https://doi.org/10.1016/j.tsep.2024.102901.

References

[1] S. Chowdhury, Y. Nirsanametla, M. Muralidhar, S. Bag, C.P. Paul, K.S. Bindra, Identification of modes of welding using parametric studies during ytterbium fiber laser welding, J. Manuf. Process 57 (2020) 748–761, https://doi.org/10.1016/j.jmapro.2020.07.038.

[2] J. Blackburn, "Laser welding of metals for aerospace and other applications," in: *Welding and Joining of Aerospace Materials*, Elsevier, 2012, pp. 67–94. doi: 10.1016/b978-0-12-819140-8.00003-1.

[3] T. Sonar, V. Balasubramanian, S. Malarvizhi, T. Venkateswaran, D. Sivakumar, "An overview on welding of Inconel 718 alloy - Effect of welding processes on microstructural evolution and mechanical properties of joints," Apr. 01, 2021, *Elsevier Inc.* doi: 10.1016/j.matchar.2021.110997.

[4] S.G.K. Manikandan, D. Sivakumar, M. Kamaraj, *Welding the Inconel 718 Superalloy*. Elsevier, 2019. doi: 10.1016/C2018-0-01653-9.

[5] M. Fisk, A. Lundbäck, Simulation and validation of repair welding and heat treatment of an alloy 718 plate, Finite Elem. Anal. Des. 58 (2012) 66–73, https://doi.org/10.1016/j.finel.2012.04.002.

[6] X. He, "Finite element analysis of laser welding: A state of art review," Dec. 01, 2012. doi: 10.1080/10426914.2012.709345.

[7] A.P. Mackwood, R.C. Crafer, Thermal modelling of laser welding and related processes: a literature review, Opt. Laser Technol. 37 (2) (2005) 99–115, https://doi.org/10.1016/j.optlastec.2004.02.017.

[8] M. Sheikhi, F. Malek Ghaini, H. Assadi, "Prediction of solidification cracking in pulsed laser welding of 2024 aluminum alloy," *Acta Mater*, vol. 82, pp. 491–502, Jan. 2015, doi: 10.1016/j.actamat.2014.09.002.

[9] H. Ki, P. S. Mohanty, J. Mazumder, "Modeling of Laser Keyhole Welding: Part I. Mathematical Modeling, Numerical Methodology, Role of Recoil Pressure, Multiple Reflections, and Free Surface Evolution.".

[10] H. Ki, P. S. Mohanty, J. Mazumder, "Modeling of Laser Keyhole Welding: Part II. Simulation of keyhole evolution, velocity, temperature profile, and Experimental Verification.".

[11] F. Farrokhi, B. Endelt, M. Kristiansen, A numerical model for full and partial penetration hybrid laser welding of thick-section steels, Opt. Laser Technol. 111 (2019) 671–686, https://doi.org/10.1016/j.optlastec.2018.08.059.

[12] L.J. Zhang, J.X. Zhang, A. Gumenyuk, M. Rethmeier, S.J. Na, Numerical simulation of full penetration laser welding of thick steel plate with high power high brightness laser, J. Mater. Process Technol. 214 (8) (2014) 1710–1720, https://doi.org/10.1016/j.jmatprotec.2014.03.016.

[13] Y. Ai, S. Han, Y. Yan, An interpolation-based transient solidification conditions model for numerical calculation of grain growth during laser welding, Therm. Sci. Eng. Prog. 47 (2024), https://doi.org/10.1016/j.tsep.2023.102259.

[14] B. Fotovvati, S. F. Wayne, G. Lewis, E. Asadi, "A review on melt-pool characteristics in laser welding of metals," 2018, *Hindawi Limited*. doi: 10.1155/2018/4920718.

[15] Z.S. Saldi, A. Kidess, S. Kenjereš, C. Zhao, I.M. Richardson, C.R. Kleijn, Effect of enhanced heat and mass transport and flow reversal during cool down on weld pool shapes in laser spot welding of steel, Int. J. Heat Mass Transf. 66 (2013) 879–888, https://doi.org/10.1016/j.ijheatmasstransfer.2013.07.085.

[16] Y. Feng et al., "Simulation and experiment for dynamics of laser welding keyhole and molten pool at different penetration status," 2021, doi: 10.1007/s00170-020-06489-y/Published.

[17] G.M. Oreper, AN and D. J. Szekely, "Heat- and fluid-flow phenomena in weld pools," 1984.

[18] A. Ebrahimi, C. R. Kleijn, I.M. Richardson, "Numerical study of molten metal melt pool behaviour during conduction-mode laser spot melting," J. Phys. D Appl Phys, vol. 54, no. 10, Mar. 2021, doi: 10.1088/1361-6463/abca62.

[19] Z. Li, K. Rostam, A. Panjehpour, M. Akbari, A. Karimipour, S. Rostami, Experimental and numerical study of temperature field and molten pool dimensions in dissimilar thickness laser welding of Ti6Al4V alloy, J. Manuf. Process 49 (2020) 438–446, https://doi.org/10.1016/j.jmapro.2019.11.024.

[20] M. Shehryar Khan, S. I. Shahabad, M. Yavuz, W. W. Duley, E. Biro, and Y. Zhou, "Numerical modelling and experimental validation of the effect of laser beam defocusing on process optimization during fiber laser welding of automotive press-hardened steels," *J Manuf Process*, vol. 67, pp. 535–544, Jul. 2021, doi: 10.1016/j.jmapro.2021.05.006.

[21] I. Hernando, J.I. Arrizubieta, A. Lamikiz, E. Ukar, "Numerical model for predicting bead geometry and microstructure in laser beam welding of inconel 718 sheets," *Metals (Basel)*, vol. 8, no. 7, Jul. 2018, doi: 10.3390/met8070536.

[22] A. Jayanthi, K. Venkataramanan, K. S. Kumar, "An overview of the experimental techniques for characterization of laser-welded metal joints," in: *Materials Today: Proceedings*, Elsevier Ltd, 2020, pp. 572–581. doi: 10.1016/j.matpr.2020.08.470.

[23] I. Granell, A. Ramos, A. Carnicero, A. González-Marcos, and F. Czerwinski, "A Geometry-Based Welding Distortion Prediction Tool," *Materials 2021, Vol. 14, Page 4789*, vol. 14, no. 17, p. 4789, Aug. 2021, doi: 10.3390/MA14174789.

[24] Y. Jia, Y. Saadlaoui, H. Hamdi, J. Sijobert, J.C. Roux, J.M. Bergheau, An experimental and numerical case study of thermal and mechanical consequences induced by laser welding process, Case Stud. Therm. Eng. 35 (2022) 102078, https://doi.org/10.1016/J.CSITE.2022.102078.

[25] M. Wei, W.J. Ding, G. Vastola, Y.-W. Zhang, Quantitative study on the dynamics of melt pool and keyhole and their controlling factors in metal laser melting, Addit. Manuf. 54 (2022) 102779, https://doi.org/10.1016/j.addma.2022.102779.

[26] D. Wu *et al.*, "Progress and perspectives of in-situ optical monitoring in laser beam welding: Sensing, characterization and modeling," Mar. 01, 2022, *Elsevier Ltd*. doi: 10.1016/j.jmapro.2022.01.044.

[27] M. Luo, Y.C. Shin, Vision-based weld pool boundary extraction and width measurement during keyhole fiber laser welding, Opt Lasers Eng 64 (2015) 59–70, https://doi.org/10.1016/j.optlaseng.2014.07.004.

[28] X. Xiao, X. Liu, M. Cheng, L. Song, Towards monitoring laser welding process via a coaxial pyrometer, J. Mater. Process Technol. 277 (2020), https://doi.org/10.1016/j.jmatprotec.2019.116409.

[29] V.N. Lednev, et al., Online and in situ laser-induced breakdown spectroscopy for laser welding monitoring, Spectrochim Acta Part B at Spectrosc 175 (2021), https://doi.org/10.1016/j.sab.2020.106032.

[30] A. Ebrahimi, et al., The influence of laser characteristics on internal flow behaviour in laser melting of metallic substrates, Mater. Des. 214 (Feb. 2022) 110385, https://doi.org/10.1016/J.MATDES.2022.110385.

[31] S. M. A. Noori Rahim Abadi, Y. Mi, F. Sikström, I. Choquet, "Modelling of beam energy absorbed locally in conduction mode laser metal fusion," J. Phys. D Appl. Phys. vol. 55, no. 2, p. 025301, Oct. 2021, doi: 10.1088/1361-6463/AC296A.

[32] C. Sainte-catherine, M. Jeandin, D. Kechemair, J.-P. Ricaud, L. Sabatier, " Study of Dynamic absorptivity At 10.6 μm (CO 2) and 1.06 μm (Nd-YAG) wavelengths as a Function of Temperature ," *Le Journal de Physique IV*, vol. 01, no. C7, pp. C7-151-C7-157, Dec. 1991, doi: 10.1051/jp4:1991741.

[33] J. Zielinski, "A holistic approach to understand laser additive manufacturing from melt pool to microstructure = Ein ganzheitlicher Ansatz zum Verständnis der Laser basierten additiven Fertigung vom Schmelzbad bis zur Mikrostruktur," 2022.

[34] A. Ebrahimi, M.J.M. Hermans, Laser butt welding of thin stainless steel 316L sheets in asymmetric configurations: a numerical study, J. Adv. Joining Processes 8 (2023) 100154, https://doi.org/10.1016/J.JAJP.2023.100154.

[35] S. Katayama, Handbook of Laser Welding Technologies, 1st ed., Woodhead Publishing, 2013.

[36] J.C. Heigel, P. Michaleris, E.W. Reutzel, Thermo-mechanical model development and validation of directed energy deposition additive manufacturing of Ti-6Al-4V, Addit. Manuf. 5 (2015) 9–19, https://doi.org/10.1016/j.addma.2014.10.003.

[37] J. Xu, Y. Rong, Improving the prediction accuracy of thermal finite element analysis for laser welding through an automated optimization method, Int. J. Adv. Manuf. Technol. 123 (5–6) (2022) 1657–1668, https://doi.org/10.1007/S00170-022-10268-2/TABLES/6.

[38] "HAYNES ® 718 alloy," 2020.

[39] K. Mills, "Ni - IN718," *Recommended Values of Thermophysical Properties for Selected Commercial Alloys*, vol. 5, no. 4, pp. 181–191, 2002.

[40] G. Buvanashekaran, N. Siva Shanmugam, K. Sankaranarayanasamy, R. Sabarikanth, "A study of laser welding modes with varying beam energy levels," in: *Proc Inst Mech Eng C J Mech Eng Sci*, vol. 223, no. 5, pp. 1141–1156, May 2009, doi: 10.1243/09544062JMES1177.

[41] O. Murua, J.I. Arrizubieta, A. Lamikiz, L. Galdos, Laser welding for stamping blank reinforcement: signal monitoring for digital certification, Procedia CIRP 111 (2022) 536–540, https://doi.org/10.1016/J.PROCIR.2022.08.086.

[42] Z. Luo, Y. Zhao, A survey of finite element analysis of temperature and thermal stress fields in powder bed fusion Additive Manufacturing, Addit. Manuf. 21 (2018) 318–332, https://doi.org/10.1016/J.ADDMA.2018.03.022.

[43] M. Courtois, M. Carin, P. Le Masson, S. Gaied, and M. Balabane, "Guidelines in the experimental validation of a 3D heat and fluid flow model of keyhole laser welding," Mar. 16, 2016, *Institute of Physics Publishing*. doi: 10.1088/0022-3727/49/15/155503.

[44] F. Giudice, A. Sili, "Validation of a Theoretical Model for Laser Welding Thermal Field by Multi-Physics Numerical Simulation," *Metals (Basel)*, vol. 13, no. 12, Dec. 2023, doi: 10.3390/met13122020.